The effective connectivity of the human hippocampal memory system

Supplementary Material

Edmund T. Rolls[1, 2, 6*], Gustavo Deco[3,4], Chu-Chung Huang[5], Jianfeng Feng[2,6]

Cerebral Cortex (2022) doi: 10.1093/cercor/bhab442

1. Oxford Centre for Computational Neuroscience, Oxford, UK
2. Department of Computer Science, University of Warwick, Coventry, UK
3. Center for Brain and Cognition, Computational Neuroscience Group, Department of Information and Communication Technologies, Universitat Pompeu Fabra, Roc Boronat 138, Barcelona, 08018, Spain Brain and Cognition, Pompeu Fabra University, Barcelona, Spain.
4. Institució Catalana de la Recerca i Estudis Avançats (ICREA), Universitat Pompeu Fabra, Passeig Lluís Companys 23, Barcelona, 08010, Spain.
5. Institute of Cognitive Neuroscience, School of Psychology and Cognitive Science, East China Normal University, Shanghai, China
6. Institute of Science and Technology for Brain Inspired Intelligence, Fudan University, Shanghai, China

*Corresponding author information:
Professor Edmund T. Rolls,
Department of Computer Science, University of Warwick, Coventry CV4 7AL, UK.
Email: Edmund.Rolls@oxcns.org
URL: https://www.oxcns.org
https://orcid.org/0000-0003-3025-1292

Modified version of the HCP-MMP1 atlas

The atlas used to define brain regions was the HCP-MMP1 atlas (Glasser et al. 2016), converted into volumetric space and modified as follows as described in detail elsewhere to produce the HCPex atlas (Huang et al. 2021a). First, the hippocampus and subiculum were defined as separate regions, using the template provided by Winterburn et al (2013). In our list of areas, shown in Table S1, the new hippocampal region was allocated into the hippocampal slot in the HCP list. The subiculum appears later in the list as a new area. Other new areas in the HCPex atlas (Huang *et al.* 2021a) include the thalamus, putamen, globus pallidus external segment, globus pallidus internal segment, amygdala, and nucleus accumbens, all defined using the template from the CIT168 reinforcement learning atlases (Pauli et al. 2018).

In the HCP-MMP1 atlas, each region has its RegionID, which we show in Table S1. Detailed information about the regions is available in the Supplementary Material File NIHMS68870-supplement-Neuroanatomical_Supplementary_Results.pdf provided by Glasser et al (2016). In that Supplementary Material file, a grouping of the regions is suggested based on geographic proximity and functional similarities, and this grouping is shown in the column labelled CortexID in Table S1. That has led to a different ordering of the regions, which we show in Table S1, with the original regionIDs from the HCP-MMP1 atlas shown in the column headed 'regionID'. This reordered version of the HCP-MMP1 atlas is described by Dr Dianne Patterson of the University of Arizona at https://neuroimaging-core-docs.readthedocs.io/en/latest/pages/atlases.html, where the following supporting files used to help generate Table S1 are available: HCP-MMP1_UniqueRegionList.csv and Glasser_2016_Table.xlsx. We made file HCPMMP_CortexID_Ordering.xlsx from this, and this is available from the present authors, though this information is available with the released version of the HCPex atlas (Huang *et al.* 2021a) with the code available at https://www.oxcns.org. The connectivity matrices shown in the present paper (e.g. Figs. 2 and 3) used the ordering shown in Table S1 with the subiculum inserted after the hippocampus.

Table S1. Regions defined in the modified Human Connectome Project atlas (Glasser *et al.* 2016). L=left hemisphere, R=right. The column 'Reordered region ID' is that used in the Figures in this paper, and is a reordering of that based on suggestions in the Supplementary Information of Glasser et al (2016). In that Supplementary Information, the 360 regions are grouped based on geographic proximity and functional similarities, which was reorganized and provided by Dr Dianne Patterson of the University of Arizona at https://neuroimaging-core-docs.readthedocs.io/en/latest/pages/atlases.html with the HCP-MMP1_UniqueRegionList.csv and is shown in the column labelled CortexID in Table S1. The volumes are in mm^3. This modified atlas with the reordering is described elsewhere (Huang *et al.* 2021a). The subiculum was an additional area to the 180 shown here.

Reordered ID (L, R)	Region	RegionLongName	Cortical Division	Cortex ID	Original ID	Voxel numbers ($1mm^3$) (L,R)
1, 181	V1	Primary_Visual_Cortex	Primary_Visual	1	1	13812, 13406
2, 182	V2	Second_Visual_Area	Early_Visual	2	4	9515, 9420
3, 183	V3	Third_Visual_Area	Early_Visual	2	5	7106, 7481
4, 184	V4	Fourth_Visual_Area	Early_Visual	2	6	4782, 4537
5, 185	IPS1	IntraParietal_Sulcus_Area_1	Dorsal_Stream_Visual	3	17	1751, 1750
6, 186	V3A	Area_V3A	Dorsal_Stream_Visual	3	13	2191, 2212
7, 187	V3B	Area_V3B	Dorsal_Stream_Visual	3	19	639, 731
8, 188	V6	Sixth_Visual_Area	Dorsal_Stream_Visual	3	3	1402, 1559
9, 189	V6A	Area_V6A	Dorsal_Stream_Visual	3	152	904, 734
10, 190	V7	Seventh_Visual_Area	Dorsal_Stream_Visual	3	16	1005, 1041
11, 191	FFC	Fusiform_Face_Complex	Ventral_Stream_Visual	4	18	3848, 4402
12, 192	PIT	Posterior_InferoTemporal_complex	Ventral_Stream_Visual	4	22	1392, 1386
13, 193	V8	Eighth_Visual_Area	Ventral_Stream_Visual	4	7	1361, 1175
14, 194	VMV1	VentroMedial_Visual_Area_1	Ventral_Stream_Visual	4	153	939, 1219
15, 195	VMV2	VentroMedial_Visual_Area_2	Ventral_Stream_Visual	4	160	639, 923
16, 196	VMV3	VentroMedial_Visual_Area_3	Ventral_Stream_Visual	4	154	941, 1242
17, 197	VVC	Ventral_Visual_Complex	Ventral_Stream_Visual	4	163	2487, 2753
18, 198	FST	Area_FST	MT+_Complex	5	157	1324, 1683
19, 199	LO1	Area_Lateral_Occipital_1	MT+_Complex	5	20	619, 909
20, 200	LO2	Area_Lateral_Occipital_2	MT+_Complex	5	21	1179, 1062
21, 201	LO3	Area_Lateral_Occipital_3	MT+_Complex	5	159	438, 915
22, 202	MST	Medial_Superior_Temporal_Area	MT+_Complex	5	2	794, 1036
23, 203	MT	Middle_Temporal_Area	MT+_Complex	5	23	620, 1005
24, 204	PH	Area_PH	MT+_Complex	5	138	3453, 3205
25, 205	V3CD	Area_V3CD	MT+_Complex	5	158	876, 1222
26, 206	V4t	Area_V4t	MT+_Complex	5	156	1037, 1249
27, 207	1	Area_1	SomaSens_Motor	6	51	6590, 5925
28, 208	2	Area_2	SomaSens_Motor	6	52	4278, 4727
29, 209	3a	Area_3a	SomaSens_Motor	6	53	2247, 2286
30, 210	3b	Primary_Sensory_Cortex	SomaSens_Motor	6	9	5451, 4350
31, 211	4	Primary_Motor_Cortex	SomaSens_Motor	6	8	10776, 10254
32, 212	23c	Area_23c	ParaCentral_MidCing	7	38	2259, 2498
33, 213	24dd	Dorsal_Area_24d	ParaCentral_MidCing	7	40	2665, 2820
34, 214	24dv	Ventral_Area_24d	ParaCentral_MidCing	7	41	1076, 1349
35, 215	5L	Area_5L	ParaCentral_MidCing	7	39	2249, 2327

36, 216	5m	Area_5m	ParaCentral_MidCing	7	36	1483, 2079
37, 217	5mv	Area_5m_ventral	ParaCentral_MidCing	7	37	1651, 1996
38, 218	6ma	Area_6m_anterior	ParaCentral_MidCing	7	44	3941, 4251
39, 219	6mp	Area_6mp	ParaCentral_MidCing	7	55	3701, 3105
40, 220	SCEF	Supplementary_and_Cingulate_Eye_Field	ParaCentral_MidCing	7	43	3500, 3371
41, 221	55b	Area_55b	Premotor	8	12	2422, 1537
42, 222	6a	Area_6_anterior	Premotor	8	96	4233, 3752
43, 223	6d	Dorsal_area_6	Premotor	8	54	2916, 2909
44, 224	6r	Rostral_Area_6	Premotor	8	78	3029, 3981
45, 225	6v	Ventral_Area_6	Premotor	8	56	2075, 2516
46, 226	FEF	Frontal_Eye_Fields	Premotor	8	10	1787, 1889
47, 227	PEF	Premotor_Eye_Field	Premotor	8	11	1006, 1258
48, 228	43	Area_43	Posterior_Opercular	9	99	1889, 1678
49, 229	FOP1	Frontal_Opercular_Area_1	Posterior_Opercular	9	113	879, 932
50, 230	OP1	Area_OP1-SII	Posterior_Opercular	9	101	1275, 1072
51, 231	OP2-3	Area_OP2-3-VS	Posterior_Opercular	9	102	943, 792
52, 232	OP4	Area_OP4-PV	Posterior_Opercular	9	100	2332, 2409
53, 233	52	Area_52	Early_Auditory	10	103	725, 580
54, 234	A1	Primary_Auditory_Cortex	Early_Auditory	10	24	1023, 796
55, 235	LBelt	Lateral_Belt_Complex	Early_Auditory	10	174	820, 901
56, 236	MBelt	Medial_Belt_Complex	Early_Auditory	10	173	1242, 1236
57, 237	PBelt	ParaBelt_Complex	Early_Auditory	10	124	1719, 1439
58, 238	PFcm	Area_PFcm	Early_Auditory	10	105	1486, 1485
59, 239	RI	RetroInsular_Cortex	Early_Auditory	10	104	1149, 1334
60, 240	A4	Auditory_4_Complex	Auditory_Association	11	175	3514, 3610
61, 241	A5	Auditory_5_Complex	Auditory_Association	11	125	3346, 3881
62, 242	STGa	Area_STGa	Auditory_Association	11	123	2509, 2187
63, 243	STSda	Area_STSd_anterior	Auditory_Association	11	128	1944, 2389
64, 244	STSdp	Area_STSd_posterior	Auditory_Association	11	129	1994, 2605
65, 245	STSva	Area_STSv_anterior	Auditory_Association	11	176	1694, 1900
66, 246	STSvp	Area_STSv_posterior	Auditory_Association	11	130	2898, 2515
67, 247	TA2	Area_TA2	Auditory_Association	11	107	1518, 1726
68, 248	AAIC	Anterior_Agranular_Insula_Complex	Insula_FrontalOperc	12	112	1859, 1691
69, 249	AVI	Anterior_Ventral_Insular_Area	Insula_FrontalOperc	12	111	1446, 1792
70, 250	FOP2	Frontal_Opercular_Area_2	Insula_FrontalOperc	12	115	750, 720
71, 251	FOP3	Frontal_Opercular_Area_3	Insula_FrontalOperc	12	114	754, 614
72, 252	FOP4	Frontal_Opercular_Area_4	Insula_FrontalOperc	12	108	2522, 1678
73, 253	FOP5	Area_Frontal_Opercular_5	Insula_FrontalOperc	12	169	1297, 1365
74, 254	Ig	Insular_Granular_Complex	Insula_FrontalOperc	12	168	841, 1077
75, 255	MI	Middle_Insular_Area	Insula_FrontalOperc	12	109	2102, 1960
76, 256	PI	Para-Insular_Area	Insula_FrontalOperc	12	178	1033, 1058
77, 257	Pir	Pirform_Cortex	Insula_FrontalOperc	12	110	2287, 1856
78, 258	PoI1	Area_Posterior_Insular_1	Insula_FrontalOperc	12	167	1811, 1835
79, 259	PoI2	Posterior_Insular_Area_2	Insula_FrontalOperc	12	106	2747, 2675
80, 260	H	Hippocampus	Medial_Temporal	13	120	4283, 3626
81, 261	PreS	PreSubiculum	Medial_Temporal	13	119	1817, 1558
82, 262	EC	Entorhinal_Cortex	Medial_Temporal	13	118	2127, 2110

83, 263	PeEc	Perirhinal_Ectorhinal_Cortex	Medial_Temporal	13	122	4826, 4755
84, 264	TF	Area_TF	Medial_Temporal	13	135	3986, 4752
85, 265	PHA1	ParaHippocampal_Area_1	Medial_Temporal	13	126	1281, 1168
86, 266	PHA2	ParaHippocampal_Area_2	Medial_Temporal	13	155	783, 771
87, 267	PHA3	ParaHippocampal_Area_3	Medial_Temporal	13	127	2023, 1122
88, 268	PHT	Area_PHT	Lateral_Temporal	14	137	4182, 3410
89, 269	TE1a	Area_TE1_anterior	Lateral_Temporal	14	132	5227, 4180
90, 270	TE1m	Area_TE1_Middle	Lateral_Temporal	14	177	3339, 3429
91, 271	TE1p	Area_TE1_posterior	Lateral_Temporal	14	133	7116, 6010
92, 272	TE2a	Area_TE2_anterior	Lateral_Temporal	14	134	5691, 5753
93, 273	TE2p	Area_TE2_posterior	Lateral_Temporal	14	136	4115, 3040
94, 274	TGd	Area_TG_dorsal	Lateral_Temporal	14	131	10192, 10269
95, 275	TGv	Area_TG_Ventral	Lateral_Temporal	14	172	3694, 4515
96, 276	PSL	PeriSylvian_Language_Area	TPO	15	25	2154, 2759
97, 277	STV	Superior_Temporal_Visual_Area	TPO	15	28	2322, 2294
98, 278	TPOJ1	Area_TemporoParietoOccipital_Junction_1	TPO	15	139	2102, 3938
99, 279	TPOJ2	Area_TemporoParietoOccipital_Junction_2	TPO	15	140	1930, 2068
100, 280	TPOJ3	Area_TemporoParietoOccipital_Junction_3	TPO	15	141	1290, 1277
101, 281	7AL	Lateral_Area_7A	Superior_Parietal	16	42	2134, 2030
102, 282	7Am	Medial_Area_7A	Superior_Parietal	16	45	2995, 2379
103, 283	7PC	Area_7PC	Superior_Parietal	16	47	3151, 3415
104, 284	7Pl	Lateral_Area_7P	Superior_Parietal	16	46	1695, 1363
105, 285	7Pm	Medial_Area_7P	Superior_Parietal	16	29	1601, 1308
106, 286	AIP	Anterior_IntraParietal_Area	Superior_Parietal	16	117	1999, 2542
107, 287	LIPd	Area_Lateral_IntraParietal_dorsal	Superior_Parietal	16	95	1008, 869
108, 288	LIPv	Area_Lateral_IntraParietal_ventral	Superior_Parietal	16	48	1681, 1783
109, 289	MIP	Medial_IntraParietal_Area	Superior_Parietal	16	50	1872, 2403
110, 290	VIP	Ventral_IntraParietal_Complex	Superior_Parietal	16	49	1890, 1577
111, 291	IP0	Area_IntraParietal_0	Inferior_Parietal	17	146	1203, 1239
112, 292	IP1	Area_IntraParietal_1	Inferior_Parietal	17	145	1692, 1632
113, 293	IP2	Area_IntraParietal_2	Inferior_Parietal	17	144	2102, 1861
114, 294	PF	Area_PF_Complex	Inferior_Parietal	17	148	5457, 5251
115, 295	PFm	Area_PFm_Complex	Inferior_Parietal	17	149	8220, 8141
116, 296	PFop	Area_PF_Opercular	Inferior_Parietal	17	147	1797, 1783
117, 297	PFt	Area_PFt	Inferior_Parietal	17	116	1983, 2039
118, 298	PGi	Area_PGi	Inferior_Parietal	17	150	4791, 4970
119, 299	PGp	Area_PGp	Inferior_Parietal	17	143	2501, 3740
120, 300	PGs	Area_PGs	Inferior_Parietal	17	151	4552, 3366
121, 301	23d	Area_23d	Posterior_Cingulate	18	32	1261, 1513
122, 302	31a	Area_31a	Posterior_Cingulate	18	162	1260, 1116
123, 303	31pd	Area_31pd	Posterior_Cingulate	18	161	1428, 864
124, 304	31pv	Area_31p_ventral	Posterior_Cingulate	18	35	950, 1022
125, 305	7m	Area_7m	Posterior_Cingulate	18	30	2128, 2067
126, 306	d23ab	Area_dorsal_23_a+b	Posterior_Cingulate	18	34	1607, 1106
127, 307	DVT	Dorsal_Transitional_Visual_Area	Posterior_Cingulate	18	142	1806, 2176
128, 308	PCV	PreCuneus_Visual_Area	Posterior_Cingulate	18	27	2245, 2416

129, 309	POS1	Parieto-Occipital_Sulcus_Area_1	Posterior_Cingulate	18	31	2531, 2727
130, 310	POS2	Parieto-Occipital_Sulcus_Area_2	Posterior_Cingulate	18	15	3261, 3093
131, 311	ProS	ProStriate_Area	Posterior_Cingulate	18	121	1222, 1055
132, 312	RSC	RetroSplenial_Complex	Posterior_Cingulate	18	14	2830, 3067
133, 313	v23ab	Area_ventral_23_a+b	Posterior_Cingulate	18	33	916, 1089
134, 314	10r	Area_10r	AntCing_MedPFC	19	65	1589, 1053
135, 315	10v	Area_10v	AntCing_MedPFC	19	88	3906, 2667
136, 316	25	Area_25	AntCing_MedPFC	19	164	1911, 2135
137, 317	33pr	Area_33_prime	AntCing_MedPFC	19	58	1354, 1316
138, 318	8BM	Area_8BM	AntCing_MedPFC	19	63	3122, 3436
139, 319	9m	Area_9_Middle	AntCing_MedPFC	19	69	6338, 5881
140, 320	a24	Area_a24	AntCing_MedPFC	19	61	2085, 2152
141, 321	a24pr	Anterior_24_prime	AntCing_MedPFC	19	59	1095, 1474
142, 322	a32pr	Area_anterior_32_prime	AntCing_MedPFC	19	179	1759, 1118
143, 323	d32	Area_dorsal_32	AntCing_MedPFC	19	62	2228, 2374
144, 324	p24	Area_posterior_24	AntCing_MedPFC	19	180	2394, 2442
145, 325	p24pr	Area_Posterior_24_prime	AntCing_MedPFC	19	57	1422, 1724
146, 326	p32	Area_p32	AntCing_MedPFC	19	64	1180, 1765
147, 327	p32pr	Area_p32_prime	AntCing_MedPFC	19	60	1569, 1305
148, 328	pOFC	Posterior_OFC_Complex	AntCing_MedPFC	19	166	2486, 2836
149, 329	s32	Area_s32	AntCing_MedPFC	19	165	604, 1015
150, 330	10d	Area_10d	OrbPolaFrontal	20	72	3644, 3096
151, 331	10pp	Polar_10p	OrbPolaFrontal	20	90	1997, 2487
152, 332	11l	Area_11l	OrbPolaFrontal	20	91	3531, 3793
153, 333	13l	Area_13l	OrbPolaFrontal	20	92	2429, 1757
154, 334	47m	Area_47m	OrbPolaFrontal	20	66	799, 781
155, 335	47s	Area_47s	OrbPolaFrontal	20	94	2795, 3080
156, 336	a10p	Area_anterior_10p	OrbPolaFrontal	20	89	1964, 1748
157, 337	OFC	Orbital_Frontal_Complex	OrbPolaFrontal	20	93	4560, 5232
158, 338	p10p	Area_posterior_10p	OrbPolaFrontal	20	170	2116, 2365
159, 339	44	Area_44	Inferior_Frontal	21	74	2435, 2589
160, 340	45	Area_45	Inferior_Frontal	21	75	3762, 2962
161, 341	47l	Area_47l_(47_lateral)	Inferior_Frontal	21	76	2527, 2592
162, 342	a47r	Area_anterior_47r	Inferior_Frontal	21	77	4167, 3763
163, 343	IFJa	Area_IFJa	Inferior_Frontal	21	79	1513, 1405
164, 344	IFJp	Area_IFJp	Inferior_Frontal	21	80	960, 740
165, 345	IFSa	Area_IFSa	Inferior_Frontal	21	82	2057, 2641
166, 346	IFSp	Area_IFSp	Inferior_Frontal	21	81	1589, 1730
167, 347	p47r	Area_posterior_47r	Inferior_Frontal	21	171	2133, 1761
168, 348	46	Area_46	Dorsolateral_Prefrontal	22	84	4863, 4394
169, 349	8Ad	Area_8Ad	Dorsolateral_Prefrontal	22	68	3386, 3492
170, 350	8Av	Area_8Av	Dorsolateral_Prefrontal	22	67	4807, 5902
171, 351	8BL	Area_8B_Lateral	Dorsolateral_Prefrontal	22	70	3377, 4078
172, 352	8C	Area_8C	Dorsolateral_Prefrontal	22	73	4085, 3134
173, 353	9-46d	Area_9-46d	Dorsolateral_Prefrontal	22	86	4534, 4666
174, 354	9a	Area_9_anterior	Dorsolateral_Prefrontal	22	87	3706, 3048
175, 355	9p	Area_9_Posterior	Dorsolateral_Prefrontal	22	71	3426, 2488

176, 356	a9-46v	Area_anterior_9-46v	Dorsolateral_Prefrontal	22	85	3314, 2628
177, 357	i6-8	Inferior_6-8_Transitional_Area	Dorsolateral_Prefrontal	22	97	1764, 2418
178, 358	p9-46v	Area_posterior_9-46v	Dorsolateral_Prefrontal	22	83	2871, 4635
179, 359	s6-8	Superior_6-8_Transitional_Area	Dorsolateral_Prefrontal	22	98	1336, 2132
180, 360	SFL	Superior_Frontal_Language_Area	Dorsolateral_Prefrontal	22	26	3873, 3055

Column 1 (Reordered ID) shows the order in HCPex based on the HCP-MMP1_UniqueRegionList.csv, as described in the Methods, of the 360 cortical regions originally defined by Glasser et al (2016). The names of the cortical divisions shown in column 4 come from the same .csv file. The sixth column shows the original order used by Glasser et al (2016). Abbreviations: L=left hemisphere, R=right. MT+_Complex, MT+_Complex_and_Neighboring_Visual_Areas; SomaSens_Motor, Somatosensory_and_Motor; ParaCentral_MidCing, Paracentral_Lobular_and_Mid_Cingulate; Insula_FrontalOperc, Insular_and_Frontal_Opercular; TPO, Temporo-Parieto-Occipital_Junction; AntCing_MedPFC, Anterior_Cingulate_and_Medial_Prefrontal; OrbPolaFrontal, Orbital_and_Polar_Frontal.

Fig. S1-1. Example coronal slices showing regions defined in the HCPex atlas and added subcortical regions. The abbreviations are as in Table S1. The y values for the coronal slices are in MNI coordinates. These figures are after Huang, Rolls et al (2021a) where more details are provided, and are included here for convenience.

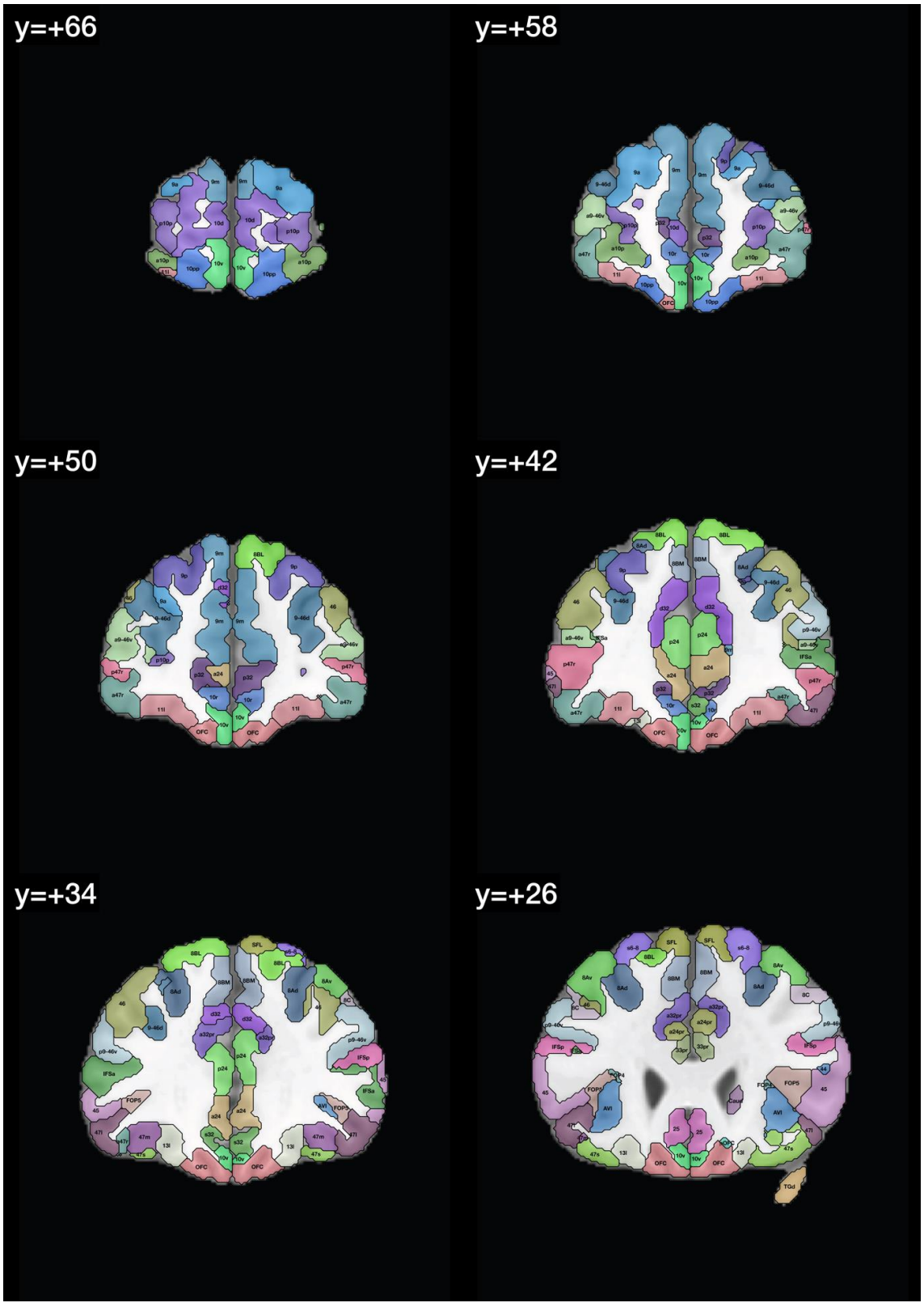

Fig. S1-2. Example coronal slices showing regions defined in the HCPex atlas and added subcortical regions. The abbreviations are as in Table S1. The y values for the coronal slices are in MNI coordinates.

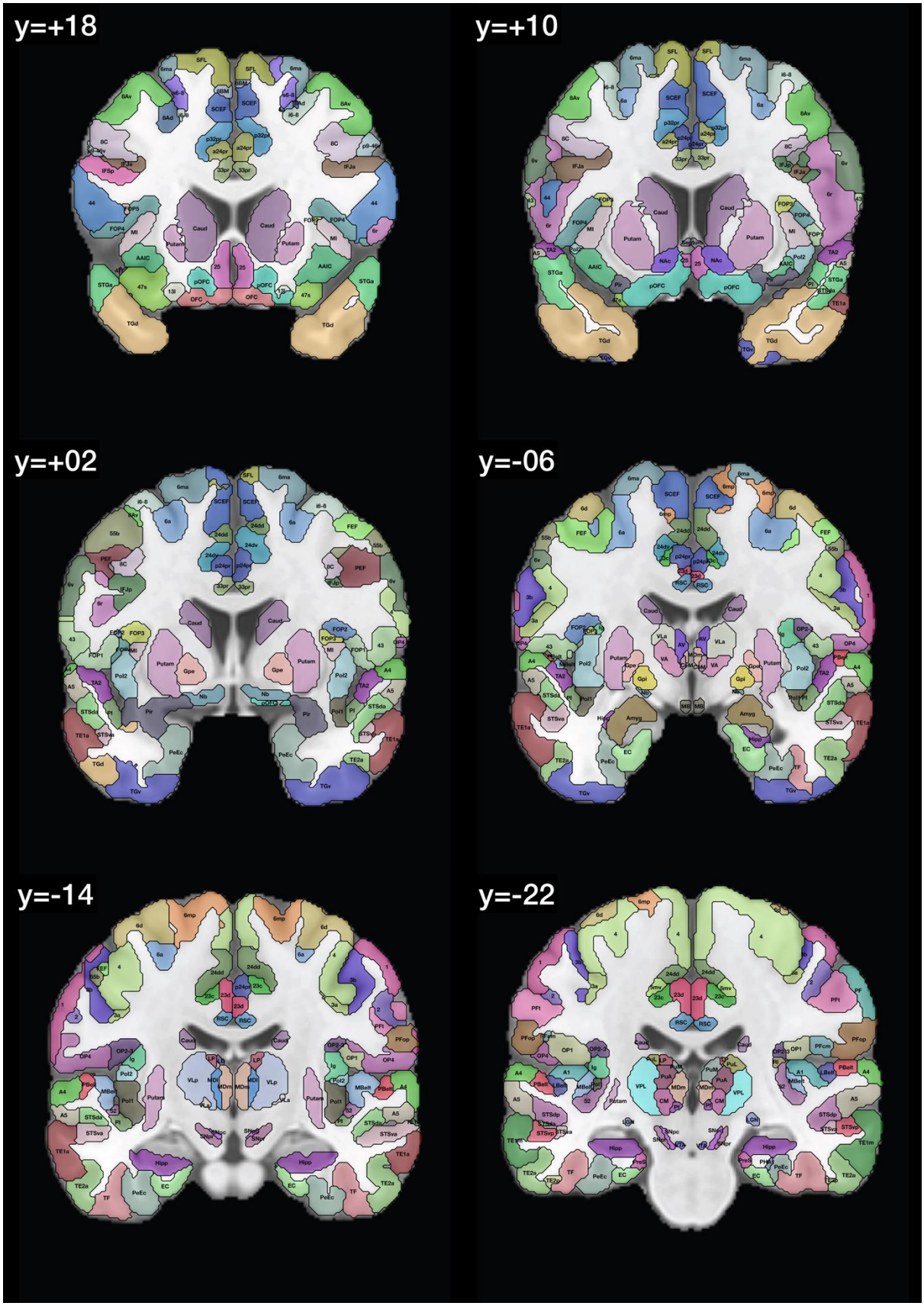

Fig. S1-3. Example coronal slices showing regions defined in the HCPex atlas and added subcortical regions. The abbreviations are as in Table S1. The y values for the coronal slices are in MNI coordinates.

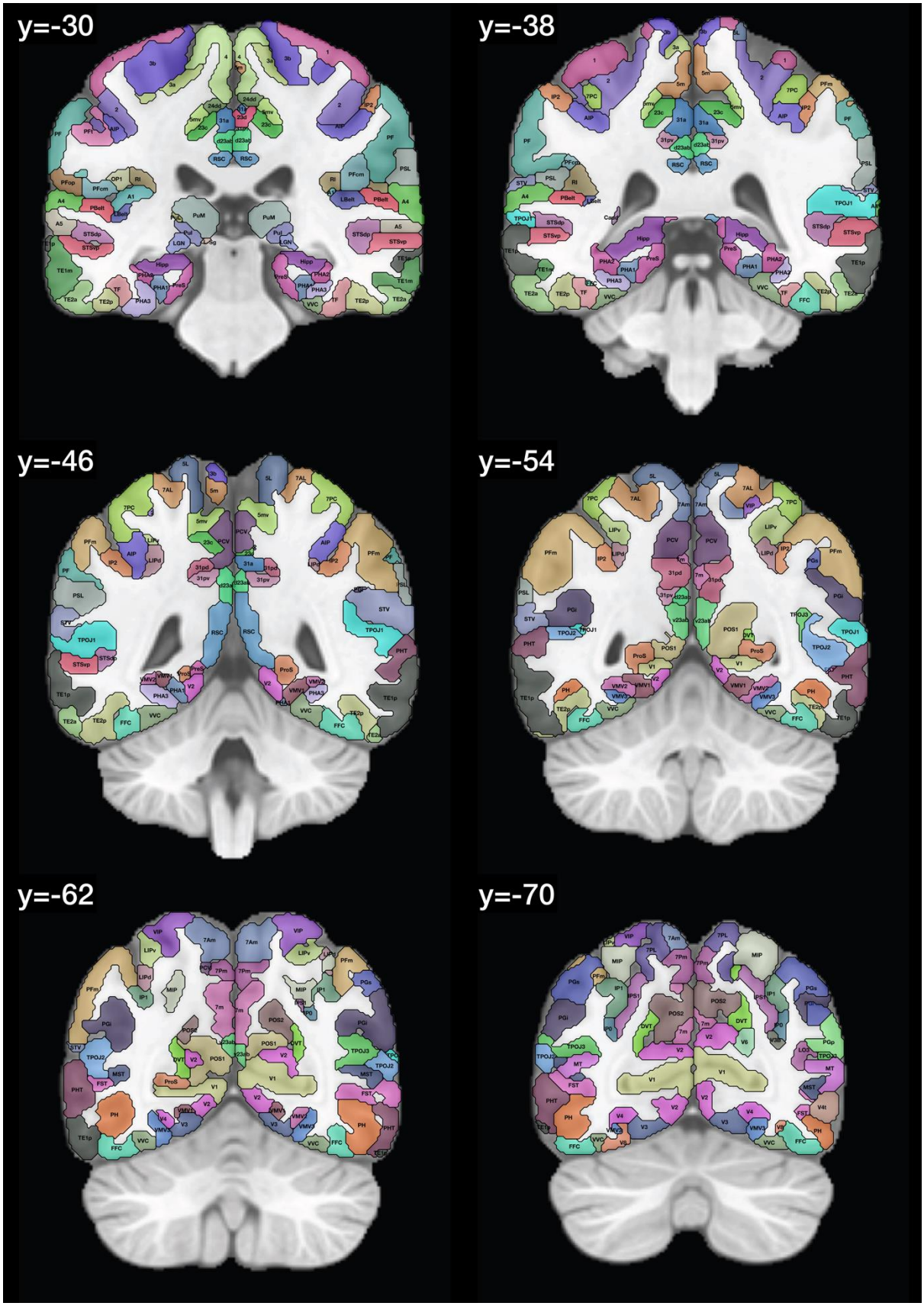

Fig. S1-4. Example coronal slices showing regions defined in the HCPex atlas and added subcortical regions. The abbreviations are as in Table S1. The y values for the coronal slices are in MNI coordinates.

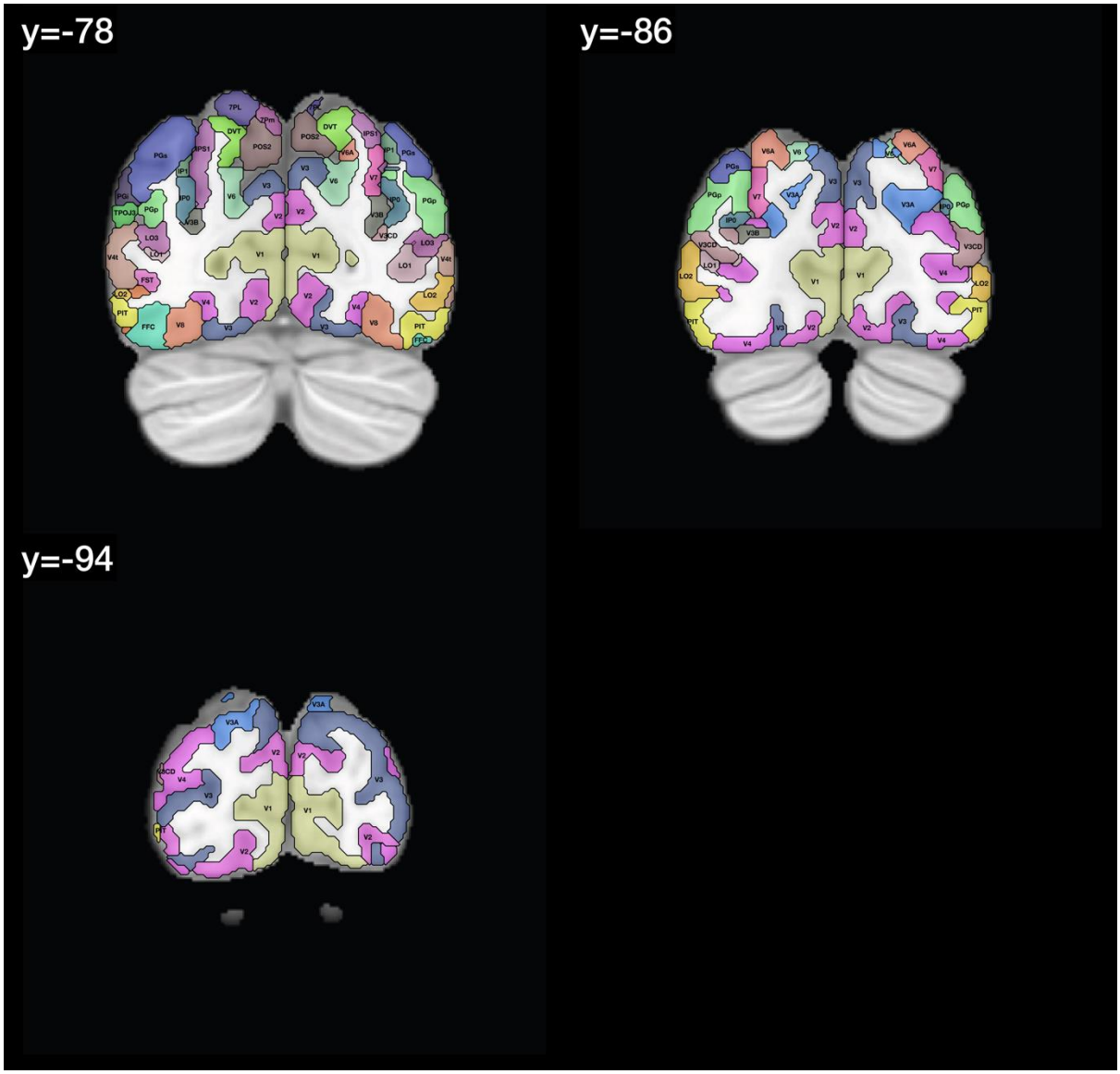

Fig. S2. Summary of connections within the human hippocampal system, as shown by diffusion tractography (Huang et al. 2021b), included here for comparison with the effective connectivity shown in Fig. 5. The numbers of streamlines between areas are indicated by the width of the arrows and the numbers. Blue indicates ventral cortical stream areas and connections that are primarily between them; and red indicates dorsal cortical stream areas and connections that are primarily between them. Where several regions are involved, for example the early visual cortical areas, the number represents the maximal value of the number of streamlines to any region. Connections with fewer than 20 streamlines are not shown in this figure. In this diagram, 'early visual cortical areas' refers to V1 to V4t in the HCP atlas; the parietal areas refer to PSL to PGs; and the temporal areas refer to TE1a to TGv, using the nomenclature and order in Table S1. (After Huang et al (2021b).)

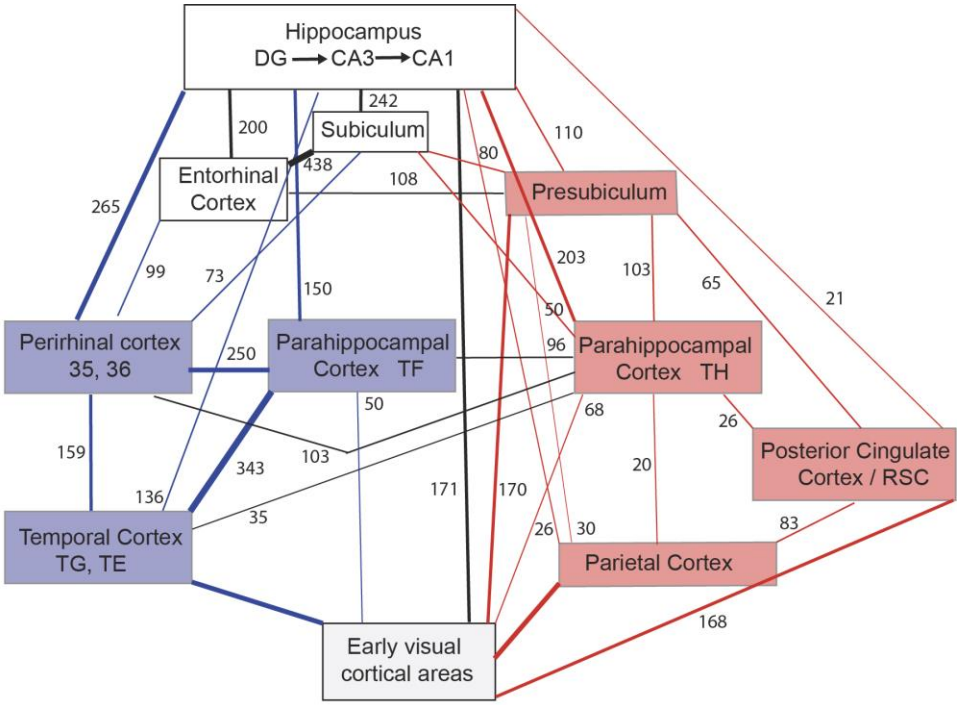

Diffusion tractography: number of streamlines

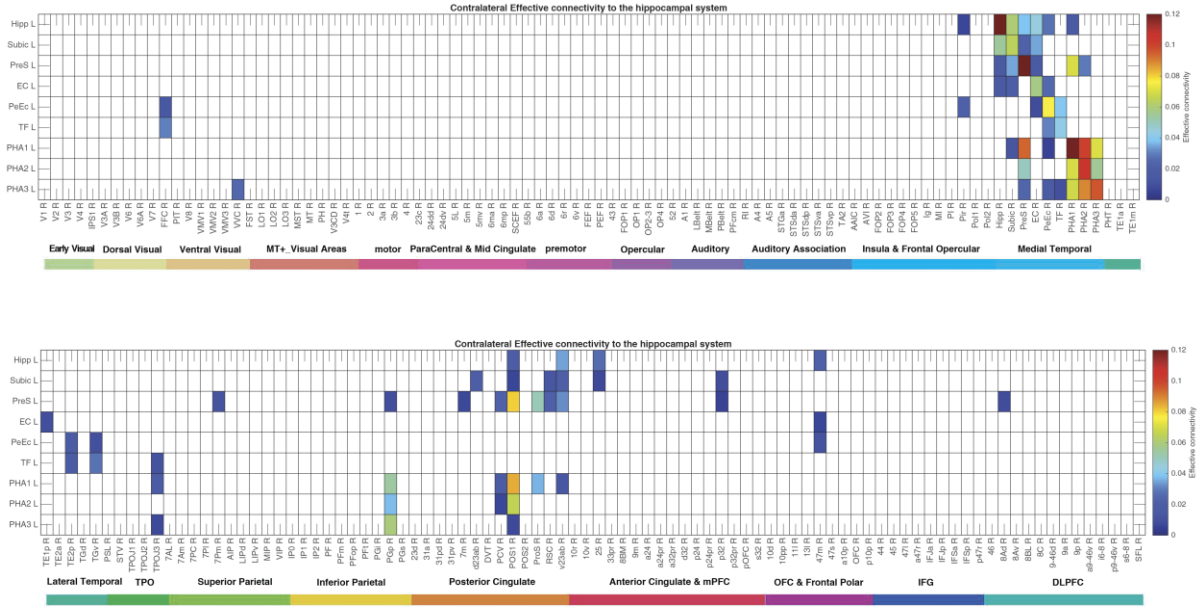

Fig. S3. Effective connectivity to the Left hippocampal system from all cortical areas in the Right (R) hemisphere. The effective connectivity is read from a column to a row. This is calculated from 172 participants in the HCP imaged at 7T. The threshold value for the effective connectivity is 0.005, with a blank indicating effective connectivity less than this, and typically 0. Hipp – hippocampus; Subic – subiculum; PreS – presubiculum; EC - entorhinal cortex; PeEc: perirhinal cortex; TF- parahippocampal area TF; PHA1-3 – parahippocampal gyrus TH areas 1-3. The abbreviations for the other brain areas are shown in Table S1, and the brain regions are shown in Fig. S1. The effective connectivity from the first set of cortical regions is shown above with the subiculum added; and from the second set of regions below.

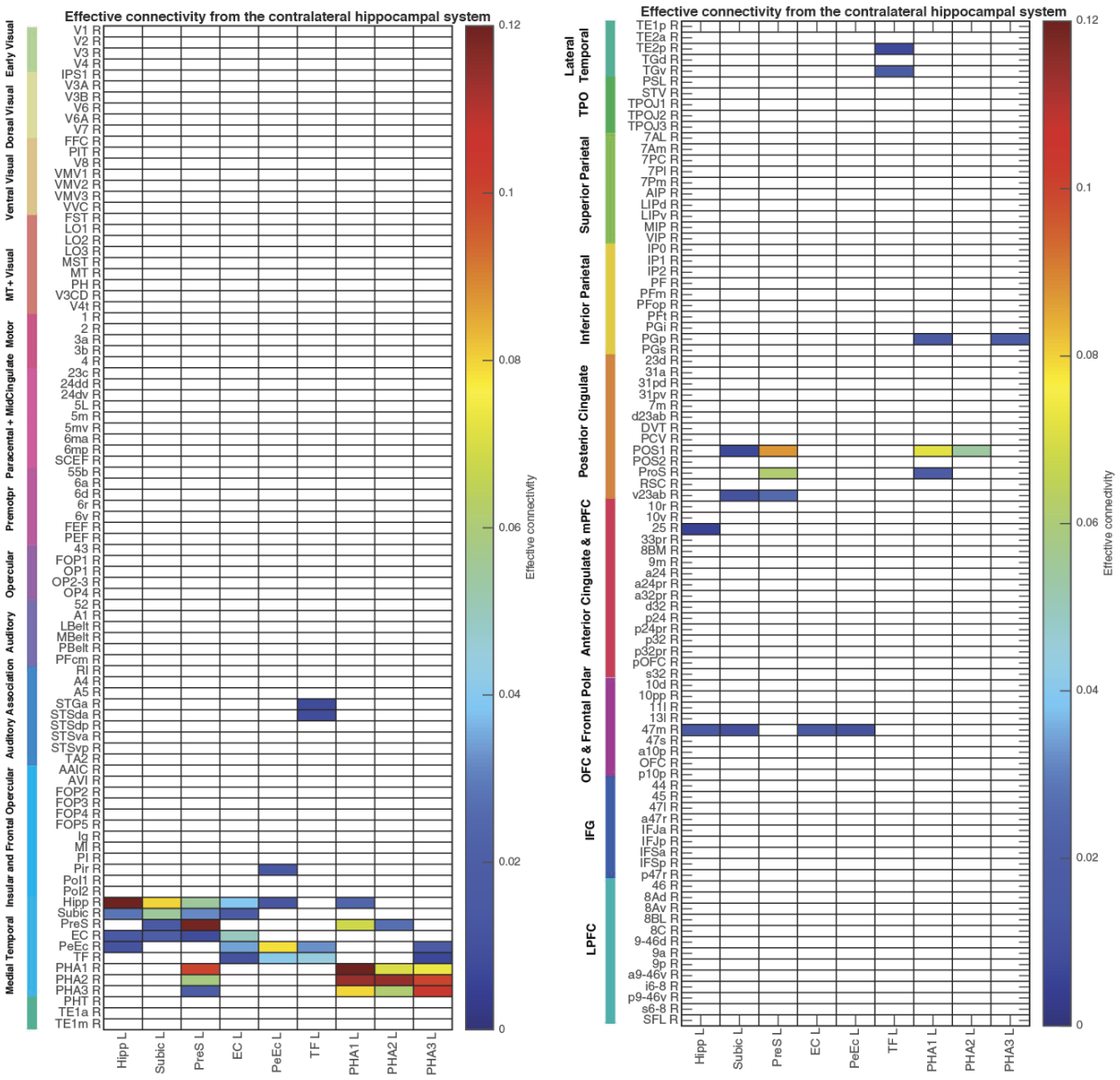

Fig. S4. Effective connectivity from the Left hippocampal system to all cortical areas in the Right hemisphere. The effective connectivity is read from a column to a row. This is calculated from 172 participants in the HCP imaged at 7T. The threshold value for the effective connectivity is 0.005. Hipp – hippocampus; Subic – subiculum; PreS – presubiculum; EC - entorhinal cortex; PeEc: perirhinal cortex; TF- parahippocampal area TF; PHA1-3 – parahippocampal gyrus TH areas 1-3. The abbreviations for the other brain regions are shown in Table S1, and the brain regions are shown in Fig. S1. The effective connectivity to the first set of cortical regions and the subiculum is shown on the left; and to the second set of regions on the right.

Effective connectivities involving early visual cortical and related areas

In order to demonstrate and check the operation of the effective connectivity algorithm, and also to show a route from early visual cortical areas to the hippocampus, Fig. S5 shows the effective connectivity of a small set of visual and related areas from the full 362x362 effective connectivity matrix for all cortical areas used in the analyses described in this paper.

It is shown in Fig. S5 that V1 has effective connectivity directed very strongly to V2, and that this is stronger than the backprojection from V2 to V1. Similarly V2 has effective connectivity directed strongly to V3. Then V4 receives most strongly from V3, with smaller effective connectivities from V2 and V1. In most cases, the backprojections are weaker. This organisation is consistent with the known connections in macaques (Markov et al. 2014), and the comparison thus provides a validation of the effective connectivity algorithm in humans. The evidence on hippocampal effective connectivity in humans shown in Figs. 2-4 and S3 and S4 is also consistent with what is known of the anatomical connectivity in macaques (reviewed in the main text and by Huang *et al.* (2021b)), and that provides further evidence that the effective connectivity algorithm described in this paper operates usefully.

However, Fig. S5 makes another interesting point about one route via which information from early cortical visual areas can reach the human hippocampus. The effective connectivity route from V1 to V2 to V3 has just been described. Fig. S5 shows that ProS receives from V1, V2 and V3. (Read along the ProS row.) Fig. S5 shows that effective connectivity is then directed from ProS to POS1 (and somewhat to the hippocampus); and that POS1 then has effective connectivity to the hippocampus. This thus provides a route for visual information to reach the hippocampus from early cortical visual areas.

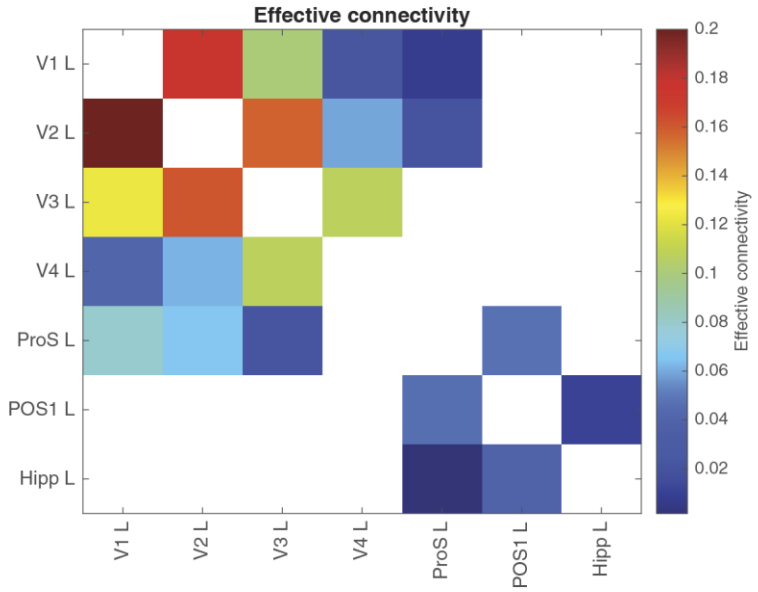

Fig. S5. Effective connectivities between some early visual cortical regions, and some other brain regions. The effective connectivities are read from column to row. The maximum effective connectivity is 0.2. These values were extracted from the same analysis described in the main text that included 362 cortical areas, and were from 172 participants imaged at 7T by the HCP. The brain areas shown are listed in Table S1 showing the cortical areas in the modified HCP atlas. V1 is the primary, striate, cortex; V2-V4 are other early visual cortical areas. ProS is a prostriate area of visual cortex; and POS1 is a nearby area in the parieto-occipital sulcus. These cortical areas are shown in Fig. S1. Blank areas had effective connectivities of 0. L indicates Left hemisphere.

Details of the Hopf Effective Connectivity algorithm

Introduction

Effective connectivity measures the effect of one brain region on another, and utilizes differences detected at different times in the signals in each connected pair of brain regions to infer effects of one brain region on another. The method used here was developed from a Hopf algorithm to enable measurement of effective connectivity between many brain areas, described by Deco et al (2019). A principle is that the functional connectivity is measured at time *t* and time *t* + *tau*, where *tau* is typically 2 s to take into account the time within which a change in the BOLD signal can occur, and then the effective connectivity model is trained by error correction until it can generate the functional connectivity matrices at time *t* and time *t* + *tau*. Further details of the algorithm, and the development that enabled it to measure the effective connectivity in each direction, are described next.

To measure the effective connectivity, we use a whole-brain model that allows us to simulate the BOLD activity across all brain regions and time. We use the so-called Hopf computational model, which integrates the dynamics of Stuart-Landau oscillators, to enable the activity (in this case the BOLD signal) of each brain region to be generated from the underlying effective connectivity in both directions between every pair of brain regions (Deco et al. 2017b). As mentioned above, we include in the model 362 cortical brain areas, or 428 when we include the 66 subcortical areas (Huang *et al.* 2021a). The local dynamics of each brain area (node) which simulate the BOLD signal are given by Stuart-Landau oscillators which express the normal form of a supercritical Hopf bifurcation, describing the transition from noisy to oscillatory dynamics (Kuznetsov 2013). Many studies have shown how the Hopf whole-brain model successfully simulates empirical electrophysiology (Freyer et al. 2011; Freyer et al. 2012), MEG (Deco et al. 2017a) and fMRI (Kringelbach et al. 2015; Deco *et al.* 2017b; Kringelbach and Deco 2020).

Overview of the effective connectivity measurement algorithm

The steps of the algorithm can be summarized as follows:

1. From the empirically measured time series of the BOLD signal for each of *N* brain areas bandpass filtered between 0.008 and 0.08 Hz we calculate the *N*x*N* empirical functional connectivity matrix FC^{emp} by the Pearson correlation between the time series of each pair of brain regions. We also create an FC^{tau_emp} *N*x*N* lagged time series matrix in which the entry for each brain region is the correlation between the BOLD signal at time *t* and *t*+*tau* calculated over the whole empirical time series. *tau* is typically set to 2 s, a minimal useful period in the BOLD signal in which a change can be detected. The lagged correlation matrix FC^{tau_emp} provides the delayed information that enables the effective connectivity to be measured in both directions between each pair of nodes.

2. The *N*x*N* effective connectivity (EC) matrix to be calculated can be initialized with zeros, or with a structural connectivity matrix obtained from for example diffusion MRI. The effective connectivity matrix is read by convention from column to row, with the effective connectivity between each pair of nodes (brain regions) 1:*N* in one direction shown in the lower left triangle, and the effective connectivity in the opposite direction in the upper right triangle. If the EC matrix is initialized with a structural connection matrix, this can have the potential advantage that nodes with no possible anatomical connection can be left at 0 and ignored in the calculations, which has the potential to increase the accuracy of the algorithm for a given number of nodes in the EC matrix, as fewer nodes need to be taken into consideration in calculating the updates to the EC matrix. If the EC matrix is initialized with zeros, this has the potential advantage that any errors in the structural connectivity matrix cannot influence the results. In practice, it has been found that with up to 362 brain areas and typical time series

for the BOLD signal and structural connectivity matrices, the effective connectivity can be calculated as well with the initialization with zeros as with the structural connectivity initialization (with correlations between the ECs calculated in these two ways typically 0.99), and therefore the initialization with zeros is used in the work described, as it makes fewer assumptions.

3. The 'natural oscillation frequency' (or 'intrinsic frequency') of each brain region or node is measured as the frequency with the peak power from the power spectrum of the BOLD signal for each node.

4. A Stuart-Landau oscillatory system with the *x* oscillatory component for each of the *N* nodes (its 'natural oscillation frequency' measured from the BOLD signal) and the *y* oscillatory components provided with the same 'natural oscillation frequency' parameters is simulated with a Hopf model. The *N* oscillators are connected by the EC matrix, and noise is injected into the system so that it just oscillates. This oscillatory system is simulated to generate simulated BOLD signals for each of the *N* brain areas.

5. The EC matrix is then updated over a series of iterations using gradient descent. The error signal is the difference between *FC,* the simulated functional connectivity matrix from the current EC matrix, and FC^{emp}, the empirically measured functional connectivity matrix, together with the corresponding difference between the simulated FC^{tau} and the empirical FC^{tau_emp} matrix.

6. The EC matrix is that which has been computed when the correlations between the simulated and empirical FC matrices, and the simulated matrix FC^{tau} and the empirical FC^{tau_emp} are at their maximum, which are typically 0.75-0.8 after 50 iterations.

The Hopf whole brain model using Stuart-Landau oscillators

The Hopf whole-brain model, which integrates the activity of Stuart-Landau oscillators expressing the activity of each brain region *i* can be expressed mathematically as follows:

$$\frac{dx_i}{dt} = \overbrace{[a_i - x_i^2 - y_i^2]x_i - \omega_i y_i}^{Local\ Dynamics} + \overbrace{G\sum_{j=1}^{N} C_{ij}(x_j - x_i)}^{Coupling} + \overbrace{\beta\eta_i(t)}^{Gaussian\ Noise} \quad (1)$$

$$\frac{dy_i}{dt} = [a_i - x_i^2 - y_i^2]y_i + \omega_i x_i + G\sum_{j=1}^{N} C_{ij}(y_j - y_i) + \beta\eta_i(t) \quad (2)$$

The pair $(x_i(t), y_i(t))$ represent the state of the dynamical system modelling brain area (node) *i*, given its interactions with all other brain areas, at a given time *t*. Equations 1 and 2 describe the dynamics of this system in Cartesian coordinates, where the $x_i(t)$ term represents the simulated BOLD signal data of brain area *i*. The values of $y_i(t)$ are relevant to the dynamics of the system but are not part of the information read out from the system.

Equations 1 and 2 describe the coupling of Stuart-Landau oscillators through an effective connectivity matrix *C*. In these equations, $\eta_i(t)$ provides additive Gaussian noise with standard deviation β. The Stuart-Landau oscillators for each brain area *i* expresses a Hopf normal form that has a supercritical bifurcation at a_i=0, so that if a_i>0 the system has a stable limit cycle with frequency $f_i = \omega_i/2\pi$ (where ω_i is the angular velocity), and when a_i<0 the system has a stable fixed point representing a low activity noisy state. The intrinsic frequency f_i of each Stuart-Landau oscillator corresponding to a brain area is in the 0.008–0.08 Hz band (*i*=1, …, 362). The intrinsic frequencies are fitted from the data, as given by the frequency with the peak power of the narrowband BOLD signals of each brain region. The coupling term in Equations 1 and 2 representing the input received in node *i* from every other node *j*, is weighted by the corresponding effective connectivity C_{ij}. The coupling is

the canonical diffusive coupling, which approximates the simplest (linear) part of a general coupling function (Deco *et al.* 2019). *G* denotes the global coupling weight, scaling equally the total input received in each brain area. With the oscillators weakly coupled, the periodic orbit of the uncoupled oscillators is preserved.

Further insight can be obtained as follows. The local dynamics of each brain region are that of a Stuart-Landau oscillator, and in Equations 1 and 2 they are shown in Cartesian coordinates. However for insight into their dynamics they can be re-expressed in polar coordinates. This is performed by taking $r_i(t)$ to be $\sqrt{x_i(t)^2 + y_i(t)^2}$, which can be interpreted as the amplitude of the Stuart-Landau oscillator modelling node *i* at time t, and $\theta_i(t)$ to be $\arctan\left(\frac{y_i(t)}{x_i(t)}\right)$, which can be interpreted as the angle by which the oscillator for node *i* has rotated by time *t*. The coordinate transform yields the following equations for the local dynamics: $\dot{r}_i = (a_i - r_i^2)r_i,\ \dot{\theta}_i = \omega_i$. Hence the local dynamics of each brain region have a rate of change of θ with respect to time (a rate of oscillation) that is constant. Similarly, we see that the rate of change of amplitude with respect to time will vanish if and only if r_i=0 or $r_i = \sqrt{a_i}$, (clearly only possible if $a_i \geq 0$). On closer inspection of the equation governing r_i we see for $a_n \leq 0$ that $\dot{r}_i$ is strictly negative for all non-zero values of r_i, hence the system converges towards a state of no amplitude. For $a_n > 0$ we see that for all non-zero values of r_i that $\dot{r}_i$ is strictly negative for $r_i > \sqrt{a_i}$ and strictly positive for $r_i < \sqrt{a_i}$, so all systems that are initialised with a non-zero amplitude converge to a state where $r_i = \sqrt{a_i}$.

To put this more formally, the system undergoes a supercritical bifurcation at a_i=0, so that if a_i>0 the system has a stable limit cycle given by $r_i = \sqrt{a_i}$, $\dot{\theta}_i = \omega_i$ (with frequency $f_i = \omega_i/2\pi$), and if a_i<0 the system has a stable fixed point $r_i = 0$. However, such asymptotic stability of the model is rather unrealistic. The value of β in the Hopf whole-brain model is the standard deviation of the Gaussian noise, and this is chosen to be sufficiently high that for a value of a_i close to the bifurcation point, such asymptotic stability is avoided. The intrinsic frequency f_i for each brain region is determined as follows. For each brain area *i*, the empirical time-series data is converted to the frequency domain using a discrete Fourier transform, and the modal frequency (that with the peak power), with the exclusion of high frequency noise, is obtained and set to be the intrinsic frequency of the given brain area. The intrinsic frequency f_i of each Stuart-Landau oscillator corresponding to a brain area is in the 0.008–0.08 Hz band (*i*=1, …, 362).

The coupling term in Equations 1 and 2 acts to align the phases and frequencies of the oscillators in connected brain regions, and represents the input received in node *i* from every other node *j* and is weighted by the corresponding effective connectivity C_{ij}. The $(x_j - x_i)$ term acts to force the dynamics of brain region *i* to more closely match and indeed synchronise with brain region *j* (with $C_{ij} > 0$).

Gradient descent to optimize the effective connectivity matrix

The effective connectivity matrix is found by gradient descent from its initial value, informed by errors in functional connectivity predictions made using the Hopf model from the current effective connectivity matrix. The gradient descent is performed in order to fit the simulated to the empirical functional connectivity (FC) pairs and the lagged FC(tau) pairs. By this, we are able to infer a non-symmetric Effective Connectivity matrix (see Gilson et al (2016)). Note that FC^{tau}, ie the lagged functional connectivity between pairs, lagged at *tau* s, breaks the symmetry and thus is fundamental for our purpose. Specifically, we compute the distance between the simulated model FC and empirical data FC^{emp}, as well as the simulated model FC^{tau} and data FC^{tau_emp} and adjust each effective connection

(entry in the effective connectivity matrix) separately with a gradient-descent approach. The model is run repeatedly with the updated effective connectivity until the fit converges towards a stable value. The update rule for an entry C_{ij} in the effective connectivity matrix is

$$C_{ij} = C_{ij} + \varepsilon\left(FC_{ij}^{emp} - FC_{ij} + FC_{ij}^{tau\_emp} - FC_{ij}^{tau}\right) \qquad (3)$$

where ϵ is a learning rate constant, and i and j are the nodes.

For the implementation, we set *tau* to be 2 s, selecting the appropriate number of TRs to achieve this. This value was chosen as a result of previous work, in which autocorrelations in the time series were taken into account (Gilson *et al.* 2016). We also note that differences in hemodynamic onsets of different brain regions are unlikely to affect the algorithm greatly, as analyzed previously (Gilson *et al.* 2016). We also found that for a value for *tau*=1 s, then the correlation of the effective connectivity matrix was 0.993 with that calculated for *tau*=2 s.

The convergence of the algorithm is illustrated in Fig. S6. The data are for 362 brain regions in the HCPex atlas extended to include the subiculum, from 172 individuals in the HCP imaged in the resting state at 7T with TR=1 s and 900 time points. The mean square error (MSE) which reflects what Equation 3 minimizes, decreases to a minimum value over about 50 iteration where MSE $= \sqrt{(FC^{emp} - FC)^2 + (FC^{tauemp} - FC)^2}$. The correlation between the empirical and the simulated functional connectivity is ccFC, and the correlation between the empirical and the simulated functional connectivity with a delay of tau=2 s is ccFCTau. These correlations between the empirical connectivities and those simulated from the estimated connectivities at each iteration are seen to reach values between 0.7 and 0.8.

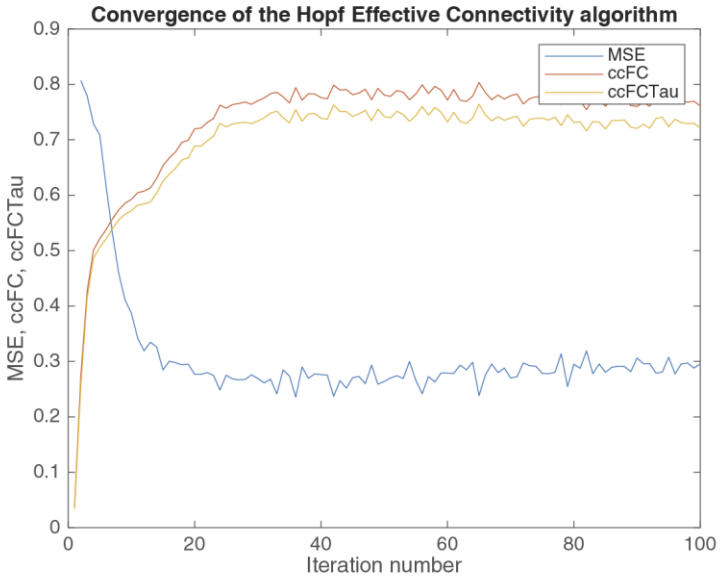

Fig. S6. Convergence of the Hopf effective connectivity algorithm. The mean square error (MSE) which reflects what Equation 3 minimizes, decreases to a minimum value over typically 20-50 iterations. The correlation between the empirical and the simulated functional connectivity is ccFC, and the correlation between the empirical and the simulated functional connectivity with a delay of *tau*=2 s is ccFCTau. The data are described above.

Interpretation of the effective connectivity measured by the Hopf algorithm

If the Hopf effective connectivity algorithm is used with an anatomical connectivity mask, then the effective connectivity for anatomically unconnected nodes (brain areas) is not updated by the effective connectivity algorithm. This enables the algorithm to measure what might be termed 'anatomical effective connectivity'. We note that in practice the anatomical maps measured with diffusion tractography are not very sparse, so that only some links are not included in the effective connectivity map that is produced. We also note that if there are any errors in the diffusion tractography connection matrix, for example some missing anatomical connection links, then those links will not be included in the effective connectivity map.

If the Hopf effective connectivity algorithm is initialized with zeros for the effective connectivity matrix, then all connectivities in the matrix can be updated by the algorithm. This ensures that there are no errors in the effective connectivity map that is generated by the algorithm due to any imperfections in the anatomical connection matrix. The effective connectivity calculated in this way reflects signals in one part of the brain that follow signals in another part of the brain with a time delay that is termed here τ (*tau*), independently of whether there is a direct anatomical connection or not. This is analogous to dynamic causal modelling and most applications of Granger causality to brain connectivity (Friston et al. 2014; Bajaj et al. 2016; Frassle et al. 2017; Razi et al. 2017), which impose no anatomical constraints on possible pathways between the nodes, i.e. the brain regions.

In practice, we have found that with the anatomical connection map we generated using diffusion tractography (Huang *et al.* 2021b), which is not very sparse, the effective connectivity matrices generated when starting with the anatomical connection matrix and the initial matrix with zeros are very similar, with typical correlations of 0.98. This is reassuring, and indicates that possible imperfections in the anatomical connection map do not produce problems in the effective connectivity matrix; and correspondingly that the Hopf effective connectivity algorithm assigns zero or close to zero effective connectivities when there is no known anatomical connection between a pair of brain regions. If a different very sparse anatomical connection matrix was used to initialize the Hopf effective connectivity algorithm, then the correlation might be lower. In practice, we prefer the initialization with zeros in the random connection matrix, as is makes fewer assumptions, but always check the results when the algorithm is initialized with an anatomical map.

The Hopf effective connectivity algorithm is different to Granger causality in its application to understanding directed connectivity between brain regions (see e.g. Ge et al. 2012; Luo et al. 2013) in a number of ways. Granger causality is applied to the time series; the Hopf effective connectivity algorithm updates a Hopf model of the effective connectivity between brain regions until it generates the functional connectivity and the lagged functional connectivity. Granger causality is typically linear; the Hopf model approach is non-linear. The Hopf model approach to effective connectivity can be constrained by an anatomical mask that takes into account connections known to be missing in the brain; the same does not apply to Granger causality applications. The Hopf effective connectivity algorithm based on a Stuart-Landau non-linear model described here is also different to a previous method of measuring effective connectivity, which used a linear approach to producing an effective connectivity matrix that could generate FC and FC^{tau} (Gilson et al. 2016; Rolls et al. 2018). It will be interesting compare these approaches in detail in the future, but at present we note that the Hopf model can generate quite good fits, with a correlation of around 0.8 to the empirical FC and FC^{tau} matrices for 428 brain regions with no anatomical constraints.

References

Bajaj S, Adhikari BM, Friston KJ, Dhamala M. 2016. Bridging the Gap: Dynamic Causal Modeling and Granger Causality Analysis of Resting State Functional Magnetic Resonance Imaging. Brain Connect 6:652-661.
Deco G, Cabral J, Woolrich MW, Stevner ABA, van Hartevelt TJ, Kringelbach ML. 2017a. Single or multiple frequency generators in on-going brain activity: A mechanistic whole-brain model of empirical MEG data. Neuroimage 152:538-550.
Deco G, Kringelbach ML, Jirsa VK, Ritter P. 2017b. The dynamics of resting fluctuations in the brain: metastability and its dynamical cortical core. Sci Rep 7:3095.
Deco G, Cruzat J, Cabral J, Tagliazucchi E, Laufs H, Logothetis NK, Kringelbach ML. 2019. Awakening: Predicting external stimulation to force transitions between different brain states. Proceedings of the National Academy of Sciences 116:18088-18097.
Frassle S, Lomakina EI, Razi A, Friston KJ, Buhmann JM, Stephan KE. 2017. Regression DCM for fMRI. Neuroimage 155:406-421.
Freyer F, Roberts JA, Becker R, Robinson PA, Ritter P, Breakspear M. 2011. Biophysical mechanisms of multistability in resting-state cortical rhythms. J Neurosci 31:6353-6361.
Freyer F, Roberts JA, Ritter P, Breakspear M. 2012. A canonical model of multistability and scale-invariance in biological systems. PLoS Comput Biol 8:e1002634.
Friston KJ, Kahan J, Biswal B, Razi A. 2014. A DCM for resting state fMRI. Neuroimage 94:396-407.
Ge T, Feng J, Grabenhorst F, Rolls ET. 2012. Componential Granger causality, and its application to identifying the source and mechanisms of the top-down biased activation that controls attention to affective vs sensory processing. Neuroimage 59:1846-1858.
Gilson M, Moreno-Bote R, Ponce-Alvarez A, Ritter P, Deco G. 2016. Estimation of directed effective connectivity from fMRI functional connectivity hints at asymmetries in the cortical connectome. PLoS Comput Biol 12:e1004762.
Glasser MF, Coalson TS, Robinson EC, Hacker CD, Harwell J, Yacoub E, Ugurbil K, Andersson J, Beckmann CF, Jenkinson M, Smith SM, Van Essen DC. 2016. A multi-modal parcellation of human cerebral cortex. Nature 536:171-178.
Huang C-C, Rolls ET, Feng J, Lin C-P. 2021a. An extended Human Connectome Project anatomical atlas. Brain Structure and Function: doi: 10.1007/s00429-00021-02421-00426.
Huang C-C, Rolls ET, Hsu C-CH, Feng J, Lin C-P. 2021b. Extensive cortical connectivity of the human hippocampal memory system: beyond the "what" and "where" dual-stream model. Cereb Cortex 31:4652-4669.
Kringelbach ML, McIntosh AR, Ritter P, Jirsa VK, Deco G. 2015. The rediscovery of slowness: exploring the timing of cognition. Trends Cogn Sci 19:616-628.
Kringelbach ML, Deco G. 2020. Brain states and transitions: insights from computational neuroscience. Cell Rep 32:108128.
Kuznetsov YA. 2013. Elements of applied bifurcation theory. New York: Springer Science & Business Media.
Luo Q, Ge T, Grabenhorst F, Feng J, Rolls ET. 2013. Attention-dependent modulation of cortical taste circuits revealed by Granger causality with signal-dependent noise PLoS Comput Biol 9:e1003265.
Markov NT, Vezoli J, Chameau P, Falchier A, Quilodran R, Huissoud C, Lamy C, Misery P, Giroud P, Ullman S, Barone P, Dehay C, Knoblauch K, Kennedy H. 2014. Anatomy of hierarchy: feedforward and feedback pathways in macaque visual cortex. J Comp Neurol 522:225-259.
Pauli WM, Nili AN, Tyszka JM. 2018. A high-resolution probabilistic in vivo atlas of human subcortical brain nuclei. Sci Data 5:180063.
Razi A, Seghier ML, Zhou Y, McColgan P, Zeidman P, Park HJ, Sporns O, Rees G, Friston KJ. 2017. Large-scale DCMs for resting-state fMRI. Netw Neurosci 1:222-241.
Rolls ET, Cheng W, Gilson M, Qiu J, Hu Z, Ruan H, Li Y, Huang CC, Yang AC, Tsai SJ, Zhang X, Zhuang K, Lin CP, Deco G, Xie P, Feng J. 2018. Effective connectivity in depression. Biol Psychiatry Cogn Neurosci Neuroimaging 3:187-197.
Winterburn JL, Pruessner JC, Chavez S, Schira MM, Lobaugh NJ, Voineskos AN, Chakravarty MM. 2013. A novel in vivo atlas of human hippocampal subfields using high-resolution 3 T magnetic resonance imaging. Neuroimage 74:254-265.